Wavelike tunneling of phonons dominates glassy thermal conductivity in crystalline $Cs_3Bi_2I_6Cl_3$

Jingyu Li,[1,3,4] Liuming Wei,[2,5] Zhuoyang Ti,[5] Le Ma,[6] Yuli Yan,[1] Guangbiao Zhang,[1,*] and Peng-Fei Liu[3,4,†]

[1]*Institute for Computational Materials Science, School of Physics and Electronics, International Joint Research Laboratory of New Energy Materials and Devices of Henan Province, Henan University, Kaifeng 475004, China*

[2]*Department of Network Security, Henan Police College, Zhengzhou 450046, China*

[3]*Institute of High Energy Physics, Chinese Academy of Sciences, Beijing 100049, China*

[4]*Spallation Neutron Source Science Center, Dongguan 523803, China*

[5]*Science Island Branch of Graduate School, University of Science and Technology of China, Hefei 230026, China*

[6]*School of Materials Science and Engineering, Nanjing University of Science and Technology, Nanjing 210094, China*

(Received 1 June 2023; accepted 17 November 2023; published 4 December 2023)

Intrinsically low lattice thermal conductivity κ_L in halide perovskites is of great interest for energy conversion applications. Here, based on first-principles calculations, we systematically study the lattice thermal conductivity of the recently synthesized layered perovskite $Cs_3Bi_2I_6Cl_3$. By using renormalized force constants extracted from lattice dynamics, our calculated κ_L is 0.227 and 0.130 $W\,m^{-1}\,K^{-1}$ along the in-plane and cross-plane directions at 300 K, respectively, which agrees well with the experimental values (0.223 and 0.209 $W\,m^{-1}\,K^{-1}$ parallel and perpendicular to the Bridgman growth direction). Meanwhile, κ_L follows a nonstandard $\kappa_L \propto T^{-0.237}$ dependence on heating, originating from the dual particle-wave behavior of heat-carrying phonons where wavelike tunneling dominates $> 72\%$ of the contribution to the total κ_L when $T > 300$ K. Further analyses imply that $Cs_3Bi_2I_6Cl_3$ manifests the coexistence of metavalent bonding, loosely bonded rattling atoms with thermally induced large-amplitude vibrations, and stereochemical lone pair activity, which induces strong anharmonicity with the soft low-lying modes, causes a mixed crystalline-liquid state, and, finally, produces unexpectedly glassy thermal conductivity. Our work pinpoints the microscopic origin of ultralow κ_L in $Cs_3Bi_2I_6Cl_3$, which is important for designing efficient materials in halide perovskites for energy conversion.

DOI: 10.1103/PhysRevB.108.224302

I. INTRODUCTION

Solid-state materials with intrinsically ultralow lattice thermal conductivity κ_L have instigated renewed interest owing to their importance in thermal management [1], thermal barrier coatings [2], and thermoelectrics [3]. Thus, understanding the mechanism of heat transport and the ability to reduce thermal conductivity are crucial to the development of energy conversion materials for the world's energy economy [4]. Most of these approaches to reducing κ_L have focused on introducing extrinsic scattering centers of all-scale and multidimensional defects into the matrix, where the resulting lattice distortion strongly strengthens the anharmonicity and significantly impedes the heat flow [5]. Although these strategies effectively lower κ_L, they often adversely affect other properties [4,5]. Alternatively, it is desirable to uncover the intrinsic lattice dynamics of a material with ultralow κ_L from both theoretical and experimental perspectives.

Up to now, a number of materials, mostly with complex atomic structures such as phonon glass electron crystals, have been proposed to hold ultralow glassy κ_L, such as skutterudites [6], clathrates [7], and tetrahedrites [8], in which anharmonic rattling modes strongly scatter heat-carrying phonons and produce low κ_L in materials. In the meantime, many liquidlike materials [9], such as $Cu_2Se_{1-x}S_x$ [10,11], $AgCrSe_2$ [12], KAg_3Se_2 [13], and argyrodites [14], have liquidlike ions that are weakly bonded and disorderly distributed inside the sublattice, leading to the observation of damaged transverse modes that decrease C_v and reduce κ_L [5,12]. Nevertheless, these crystalline compounds, in principle, have large unit cells and complex structures, and some of them incorporate a large amount of disorder [11,14]. In contrast, ultralow κ_L is relatively rare in simple crystals with well-ordered atomic structures.

Halide perovskites [15,16], spanning from organic-inorganic hybrid halides [17] to all-inorganic halide materials (such as $CsPbCl_3$ [18] and $Cs_2AgTlCl_6$ [19]), hold great promise for a diverse array of applications [16] in light-emitting diodes [20], x-ray detectors [21], field-effect transistors [22], solar cells [23], thermochromic smart windows [24], and semiconductor lasers [25]. In addition to this multifunctional nature, their reemergence as possible contenders for future thermoelectrics has received increasing interest due to their ultralow thermal conductivity coupled with decent mobility and charge carrier tunability [15]. $Cs_3Bi_2I_6Cl_3$ [26], as one of the all-inorganic metal halide perovskites, was recently synthesized and has an ultralow κ_L ($\sim$0.223 $W\,m^{-1}\,K^{-1}$ at 300 K) with glasslike temperature dependence [27]. This feature is rare in a crystalline material in the absence of impurity, disorder, and a complex cell [5]. However, fundamental study of its thermal transport is still lacking despite its practical importance. It is thus significant to provide a detailed

*Corresponding author: gbzhang@vip.henu.edu.cn

†Corresponding author: pfliu@ihep.ac.cn

atomistic understanding of ultralow κ_L in $Cs_3Bi_2I_6Cl_3$ for future applications.

In this work, we fully study the lattice thermal transport mechanism of $Cs_3Bi_2I_6Cl_3$ from the perspective of chemical bonding and lattice dynamics by means of first-principles calculations and a unified theory of the thermal transport equation [28,29] that includes both particlelike and wavelike phonon conduction. By involving anharmonic second- and third-order force constants extracted from molecular dynamics, our theoretically calculated κ_L of 0.227 $W\,m^{-1}\,K^{-1}$ coincides well with the experimental data [27] ($\sim$0.223 $W\,m^{-1}\,K^{-1}$) at 300 K. More fundamentally, the coherence contributions from wavelike tunneling of phonons are preponderant (>72%) in the heat transport process when $T \geqslant 300$ K. In-depth analysis reveals that the presence of a lone pair of electrons of I atoms; metavalent bonding; and rattling vibrations of Cs, I, and Cl atoms in $Cs_3Bi_2I_6Cl_3$ cause strong lattice anharmonicity, with the resulting existence of low-energy Einstein modes and thermally induced part-liquid states with an even flow of species atoms. These results will provide a valuable reference for further exploring thermal transport in halide perovskites.

II. RESULTS AND DISCUSSION

$Cs_3Bi_2I_6Cl_3$ crystallizes in the trigonal space group $P\bar{3}m1$ (No. 156) as a new member of the layered halide perovskites [26]. It is isostructural to zero-dimensional α-$Cs_3Sb_2I_9$ [30] and $Cs_3Bi_2Br_9$ [31] but in the two-dimensional (2D) structure with corner-connected $[Bi_2Cl_6I_3]^{3-}$ octahedra manifested in one layer in the inset of Fig. 1(d). Our optimized lattice constants of $a = 8.43$ Å and $c = 10.29$ Å coincide with the refined values ($a = 8.24$ Å and $c = 10.03$ Å) [27] and the single crystal x-ray powder diffraction data ($a = 8.24$ Å and $c = 10.02$ Å) [26]. The Bi-I and Bi-Cl bond lengths in $Cs_3Bi_2I_6Cl_3$ are 2.97 and 2.94 Å, respectively, which are nearly identical and agree well with the experimental values [26]. Nevertheless, we should note that each octahedron is slightly distorted since it comprises three capping iodine atoms and three bridging chlorine atoms.

Similar to other halide perovskites [33,34], the phonon dispersion of $Cs_3Bi_2I_6Cl_3$ based on the harmonic approximation exhibits multiple imaginary phonon branches in Fig. 1(a). The anharmonic phonon dispersion at 300 K calculated using the TDEP software is also plotted in Fig. 1(a). Clearly, we see that the frequencies of the unstable modes sensitively change with the renormalized force constant by capturing the effect of higher-order anharmonic phonon-phonon interactions from molecular dynamics. Due to the large frequency shifts, there is no imaginary frequency observed in $Cs_3Bi_2I_6Cl_3$ at 300 K in the whole Brillouin zone, indicating its inherent dynamic stability [35] and strong anharmonicity. Figure 1(b) displays the calculated total spectral function $S(\mathbf{q}, \Omega)$ from three-phonon scattering and mass imperfections (at 300 K) along the high-symmetry directions in the Brillouin zone. Usually, the very broad linewidth of the phonon bands points to their short lifetimes. Due to the strong phonon-phonon scattering, the character of the dispersion disappears, and most of branches merge [36]. Compared to the phonon dispersions in Fig. 1(a), $S(\mathbf{q}, \Omega)$ clearly produces the collapse of softened modes

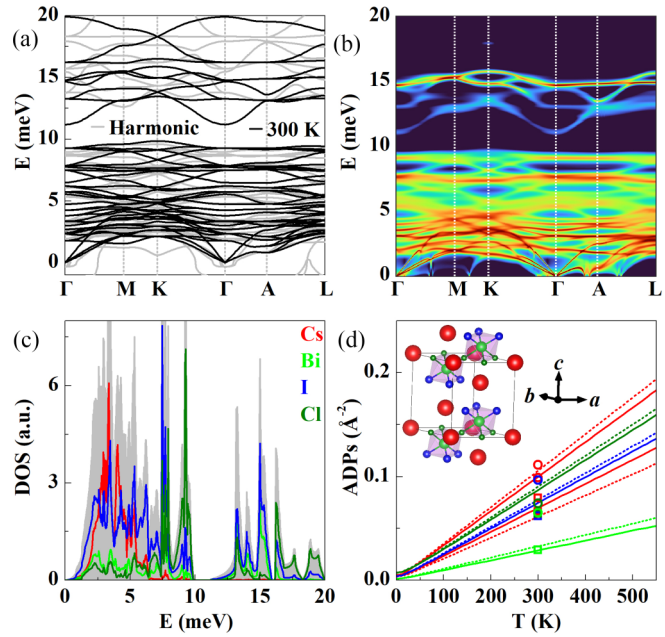

FIG. 1. (a) Harmonic (gray) and anharmonic (black; 300 K) phonon dispersions. The anharmonic phonons are calculated using the temperature-dependent effective potential theory. (b) Calculated spectral function $S(\mathbf{q}, \Omega)$ of $Cs_3Bi_2I_6Cl_3$ at 300 K. The color saturation increases linearly from zero to the maximum value. The finite width of the bands is given by physical lifetimes due to phonon-phonon scattering. (c) The corresponding phonon density of states at 300 K. (d) Theoretical (lines) and experimental (squares for Ref. [26] and circles for Ref. [27]) atom displacement parameters for Cs (red), Bi (green), I (blue), and Cl (olive) atoms in $Cs_3Bi_2I_6Cl_3$. The dashed lines indicate the in-plane direction, while the solid lines show the cross-plane direction. Inset: crystal structure of $Cs_3Bi_2I_6Cl_3$ created by VESTA [32].

close to 0 meV along the high-symmetry lines, although the unstable modes have been anharmonically stabilized. This demonstrates the giant phonon anharmonicity in $Cs_3Bi_2I_6Cl_3$. Figure 1(c) shows the anharmonic phonon density of states of $Cs_3Bi_2I_6Cl_3$ at 300 K. The collective motions of Cs and I atoms dominate the acoustic modes and low-frequency optical modes and cause giant anharmonicity, as discussed below, while the high-frequency phonon branches above the phonon gap are governed primarily by the motions of Bi, I, and Cl atoms. Notably, the vibrations of I atoms contribute over the whole frequency range, indicating that I atoms form the delocalized bonding with Bi atoms which is derived from the electronic localization function analysis in Fig. 6. This easily softens the crystal lattice and enhances the anharmonicity of the title material.

Generally, introducing low-energy Einstein modes is an effective way to scatter heat-carrying phonons and, accordingly, reduce κ_L [37,38]. As shown in Figs. 1(a)–1(c), many flattened low-energy optical branches, with suppressed group velocity, cut off the acoustic phonons from 1.5 to 4 meV. These soft vibrations, which behave like Einstein oscillators, are confirmed by the existence of three Einstein modes (1.65 meV for I atoms, 3.52 meV for Cs atoms, and 6.63 meV for I and Cl atoms) in the fitted Debye-Einstein model, as indi-

TABLE I. The atom displacement parameters (ADPs; in $Å^2$) extracted from Ref. [26], nearest-neighbor distances R_{NN} (in Å), and Lindemann parameters δ for Cs, Bi, I, and Cl atoms in $Cs_3Bi_2I_6Cl_3$ at 300 K. In addition, the transferred (e_T) and shared (e_S) charges between atoms in $Cs_3Bi_2I_6Cl_3$ are also provided.

	Atom			
	Cs	Bi	I	Cl
ADP	0.066/0.079	0.029	0.062	0.064
R_{NN}	3.920/4.070	2.900	2.900	2.930
δ	0.066/0.069	0.059	0.086	0.086
e_T	0.809/0.807	0.956	−0.428	−0.588
	Bond			
	Cs-Cl	Cs-I	Bi-Cl	Bi-I
e_S	0.054/0.076	0.124/0.104	0.554	0.890

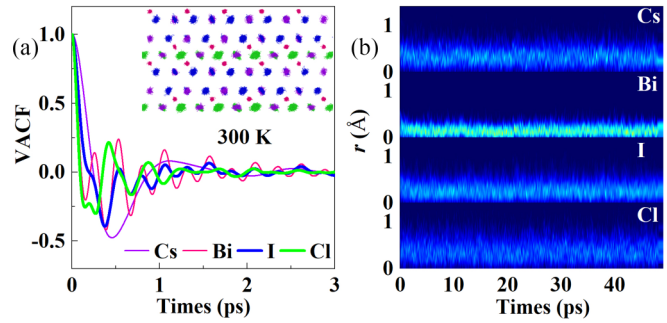

FIG. 2. (a) The decay patterns of the velocity autocorrelation function as a function of time from MD simulations for Cs, Bi, I, and Cl atoms. Inset: Trajectory of atoms in the y-z plane from MD simulations at 300 K for $Cs_3Bi_2I_6Cl_3$. (b) Calculated self-part of the van Hove correlation functions at 300 K for Cs, Bi, I, and Cl atoms.

cated in previous work [27]. They are usually associated with weakly bound atoms that randomly fluctuate as rattlers with ultralarge atom displacement parameters (ADPs) in Fig. 1(d). The experimental ADPs of atoms in $Cs_3Bi_2I_6Cl_3$ at 300 K extracted from Ref. [26] are very large (> 0.062 $Å^{-2}$) except for those of Bi atoms (0.029 $Å^{-2}$) in Table I. Such large ADPs of Cs, I, and Cl atoms indicate that they are loosely bound in the lattice, and the corresponding sublattice can even be considered to be "melted" on the basis of the Lindemann criterion of melting [39]. The Lindemann parameter δ of atoms in $Cs_3Bi_2I_6Cl_3$ is calculated to be 0.066/0.069, 0.059, 0.086, and 0.086 for Cs, Bi, I, and Cl atoms, respectively, using $\delta = \mathrm{ADP}^{1/2}/R_{NN}$, where R_{NN} is the nearest-neighbor distance. δ of I and Cl exceed the Lindemann criterion of melting (0.07 or above), while the values for Cs are in close proximity to the limit. This indicates that the sublattices of Cs, I, and Cl atoms are nearly in a liquid state. In this respect, $Cs_3Bi_2I_6Cl_3$ should have the crystal-liquid duality [40], containing both a crystalline framework and noncrystalline rattling atoms with large-amplitude random movements [41], due to the existence of hierarchical chemical bonds [42].

To validate the crystal-liquid duality in $Cs_3Bi_2I_6Cl_3$, we calculate the velocity autocorrelation function (VACF) as a function of time from molecular dynamics (MD) simulations. In Fig. 2(a), the behavior of Bi atoms follows a damped oscillating VACF as in a solid, while the VACF of Cs atoms exhibits a widely distributed and damped single-valley behavior. For I and Cl atoms, a serious deformation exists in the first valley, and the VACFs rapidly weaken in oscillation. The VACFs of Cs, I, and Cl atoms behave partially as in a liquid, whereas for the liquid-only case one single-valley minimum is present due to the large-amplitude random fluctuating behavior of these atoms [41,43]. The inset in Fig. 2(a) plots the simulated trajectory of atoms in the y-z plane of $Cs_3Bi_2I_6Cl_3$ at 300 K in MD. The oscillation amplitude for atoms goes in the order Cl > I > Cs > Bi. Although Cl, I, and Cs have large vibrational amplitudes with fluidlike diffusion, they are still constrained to around their equilibrium positions like local rattling of fillers in skutterudites [44], which is different from the well-known liquidlike materials involving site disorder of atoms, such as $AgCrSe_2$ [12], Cu_2Se [11], and argyrodites [14]. As shown in Fig. 2(b), we investigate the diffusion dynamics by calculating the self-part of the van Hove correlation function of Cs, Bi, I, and Cl atoms [45]. Figure 2(b) shows the correlation function has a constant and strong peak for each atom, clearly demonstrating the feature of ordered structures. In the meantime, it smears with large amplitudes of Cs, I, and Cl atoms and ends up with a liquid-like feature. Thus, $Cs_3Bi_2I_6Cl_3$ shows a mixed crystal-liquid state feature, which strongly deviates from the homogeneous crystalline picture of classical solids.

As previously reported, $Cs_3Bi_2I_6Cl_3$, as a solid-liquid hybrid phase, has an ultralow κ_L ($\sim$0.20 $W\,m^{-1}\,K^{-1}$ at room temperature) with glasslike temperature dependence [27]. To understand the mechanism, we calculate the unified κ_L in the framework of the Wigner formalism of quantum mechanics [28,29] by using separate solidlike (population conductivity from particlelike phonon propagation κ_p) and glasslike (coherence conductivity from wavelike phonon tunneling κ_c) terms:

$$\kappa_L = \kappa_p + \kappa_c. \tag{1}$$

In this way, κ_p coincides with the standard Peierls-Boltzmann thermal conductivity in crystals from the diagonal ($s = s'$) terms of the Wigner heat-flux operator, while the off-diagonal ($s \neq s'$) terms give rise to κ_c as described by the Allen-Feldman equation for glasses [28,29]. By considering force constant renormalization, the converged κ_L at 300 K along the in-plane direction is boosted to 0.227 $W\,m^{-1}\,K^{-1}$. We note the value agrees well with the experiment result (0.223 and 0.209 $W\,m^{-1}\,K^{-1}$ parallel and perpendicular to the Bridgman growth direction). Our calculated κ_L along its stacking direction reaches an extremely low value of 0.130 $W\,m^{-1}\,K^{-1}$: only five times that of air (0.025 $W\,m^{-1}\,K^{-1}$ at 300 K). Similar to Bi_2Te_3 [46], $Cs_3Bi_2I_6Cl_3$ exhibits highly anisotropic κ_L with a ratio of 1.74 between the in-plane and cross-plane directions due to its intrinsic layered structure with the stacking of 2D $[Bi_2I_6Cl_3]^{3-}$ layers along the crystallographic c direction. The average $\kappa_L^{\text{average}}$ of $Cs_3Bi_2I_6Cl_3$ is further averaged along the three principal crystallographic axes and is calculated to be $\sim$0.19 $W\,m^{-1}\,K^{-1}$ at 300 K, which is the same as the theoretical minimum estimated using Cahill's model [27,47]. Figure 3(a) demonstrates the coexistence of

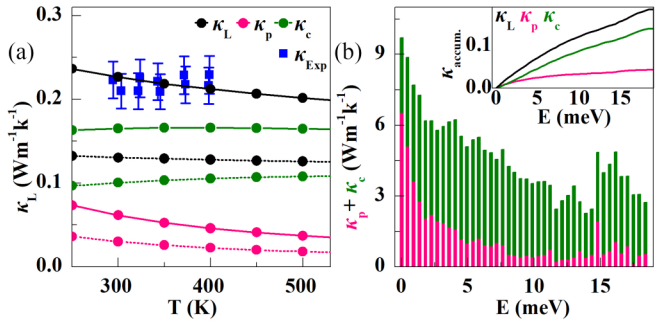

FIG. 3. (a) Calculated temperature-dependent thermal conductivity of $Cs_3Bi_2I_6Cl_3$: κ_p (pink), κ_c (olive), and κ_L (black). The solid and dotted lines indicate κ along the in-plane and cross-plane directions, respectively. The experimental results (blue) along parallel and perpendicular to Bridgman growth direction are extracted from previous work [27] for comparison. (b) Phonon-mode-resolved thermal conductivity of populations (κ_p; pink) and coherences (κ_c; olive) at 300 K. Inset: Cumulative total thermal conductivity (κ_L; black) as a sum of the population contribution (κ_p; pink) and coherence contribution (κ_c; olive) at 300 K.

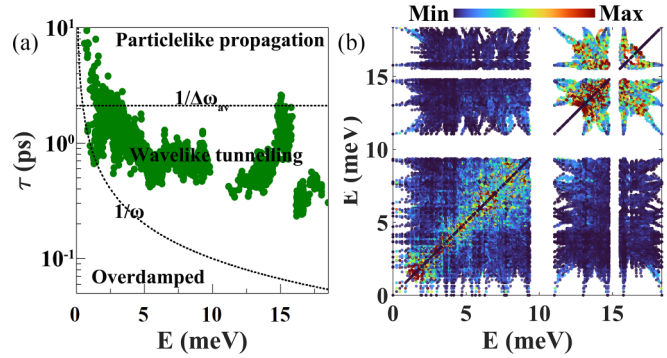

FIG. 4. (a) Phonon lifetimes $\tau(\mathbf{q})$ as a function of the energy at 300 K for $Cs_3Bi_2I_6Cl_3$. The intensity of the color depends on the density of the $\mathbf{q}$ points. (b) Two-dimensional density of states for the thermal conductivity $\kappa_{c,\omega_1\omega_2}$, which resolves how much a Zener-like coupling between two vibrational modes with frequencies ω_1 and ω_2 contributes to the coherences' conductivity.

κ_p and κ_c, and κ_c dominates $\gtrsim$70% of the total κ_L for heat conduction above 200 K. Upon heating, κ_c increases with T, while κ_p, by contrast, shows the opposite trend. This leads our calculated κ_L to a nonstandard $\kappa_L \propto T^{-0.237}$ delay and glassy feature. This nearly temperature independent κ_L is infrequent but, nevertheless, is found in some complex and strong anharmonic crystals [14,48,49]. In Fig. 3(b), we show the predominance of the coherence conductivity over the population conductivity with respect to the phonon frequency at 300 K. More specifically, the population contribution originates mainly from the low-frequency modes, while all phonons contribute to the coherence term in the random distribution. The behaviors of the two terms result in the low-energy rapid growth of κ_p and the increase of κ_c over the whole energy range in the inset in Fig. 3(b).

To analyze the strength of particlelike and wavelike conduction mechanisms, we resolve the phonon lifetime $\tau(\mathbf{q})_s$ as a function of the phonon energy at 300 K. In Fig. 4(a), three regions can be distinguished in time by the Ioffe-Regel limit ($\tau_{\text{Ioffe-Regel}} = 1/\omega$ [50]) and the Wigner limit ($\tau_{\text{Wigner}} = 1/\Delta\omega_{\text{avg}}$ [28]). Phonons with $\tau > \tau_{\text{Wigner}}$ (i.e., with a long lifetime) contribute mainly to κ_p, and phonons with $\tau_{\text{Ioffe-Regel}} < \tau < \tau_{\text{Wigner}}$ govern κ_c. When, instead, phonons are those with $\tau < \tau_{\text{Ioffe-Regel}}$, they are overdamped and require spectral-function approaches [51,52] to describe them. Unlike well-defined crystals, we note that, in $Cs_3Bi_2I_6Cl_3$, almost all of the phonons are above the Ioffe-Regel limit and below the Wigner limit in time, where the heat mainly diffuses in a wavelike fashion (73% and 77% along the in-plane and out-plane directions at 300 K) as in glasses. In addition, very few low-frequency modes appear close to $\tau_{\text{Ioffe-Regel}}$, where many low-energy optical phonons cut off acoustic phonons. These strongly localized modes, usually accompanied by avoided crossing of rattler modes, can cause resonant scattering effects and, accordingly, extremely low phonon lifetimes [53]. As a matter of fact, κ_c in Fig. 3(b) can be decoupled in terms of the pairs of coupled modes (ω_1, ω_2), as shown in Fig. 4(b). Clearly, the major contributors to κ_c locate near the diagonal of the frequency plane with quasidegenerate vibrational frequencies, which is similar to the case of harmonic glasses [28].

Astoundingly, from the analysis above, we know $Cs_3Bi_2I_6Cl_3$ has the crystal-liquid duality of ultralow thermal conductivity containing a greater than 74% glasslike heat transport contribution [18,54], which is widely different from well-defined crystals. To explicitly probe the underlying mechanism, we calculate the spherical electron localization function [55] to see hierarchical chemical bonds in $Cs_3Bi_2I_6Cl_3$. In general, iodine as a p-block element is frequently chemically active with localized lone pair electrons when it is unsaturated in bonding [56]. Naturally, lone pair electrons tend to be in one direction with a mushroomlike shape. In $Cs_3Bi_2I_6Cl_3$, each I atom is solely bonded to a Bi atom, with Cs atoms filling in the interspaces. The six nearest I atoms form a hollow octahedron which stockpiles lone pair electrons. This complex coordination environment of I atoms causes hybridized lone pair electrons to be stereochemically active in Fig. 5(a) as a ring distributed on one side of the crest angle. It will lead to the emergence of rattling atoms as well as other atoms with large-amplitude fluctuations and weakly bound bonds in $Cs_3Bi_2I_6Cl_3$, which we pointed out above. As a tool for studying chemical bonding, noncovalent interaction analysis can directly show weak atomic interactions based on the reduced density gradient (RDG) as a function of $\text{sgn}(\lambda_2)\rho$, where ρ is the electron density and $\text{sgn}(\lambda_2)$ is the sign of the second eigenvalue of the electron density Hessian matrix. In Fig. 5(b), we see that many weak interactions exist in the RDG approaching zero (<0.003 e Å^{-3}) at the critical point within the low electron density region. As a result, such weak interactions cause phonon instability with suppressed group velocity and enhanced scattering phase space [59]. To further quantify the bonding, we calculate the shared and transferred charges between atoms in $Cs_3Bi_2I_6Cl_3$ in Table I [60–62], so they can fit into a 2D map of the bonding mechanism [58]. In fact, the material studied herein lies in the region of the metavalent bond in Fig. 5(c) alongside other well-known low-κ_L thermoelectric materials [63]. This specific metavalent

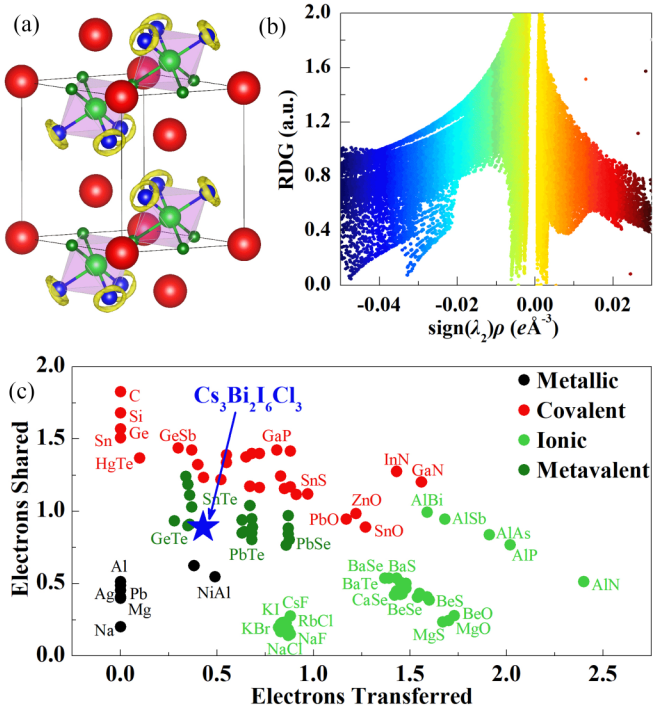

FIG. 5. (a) Calculated electronic localization function for $Cs_3Bi_2I_6Cl_3$ at an isosurface level of 0.90 e bohr^{-3}. (b) Noncovalent interaction analysis [57] based on the reduced density gradient versus the electron density multiplied by the sign of the second Hessian eigenvalue. Negative sgn(λ_2)ρ indicates attractive interactions, while positive sgn(λ_2)ρ means repulsive interactions. Weak interactions spread all over the region close to sgn(λ_2)$\rho = 0$. (c) Charge sharing vs charge transfer map, where $Cs_3Bi_2I_6Cl_3$ studied herein belongs to the metavalent bonding category with strong intrinsic phonon anharmonicity. The data for materials other than $Cs_3Bi_2I_6Cl_3$ are taken from Ref. [58].

bonding drives strong anharmonicity [64] ($\gamma = 3.35$ calculated using the TDEP software), which greatly disrupts the heat propagation and ensures glassy behavior of κ_L in $Cs_3Bi_2I_6Cl_3$.

III. CONCLUSIONS

In summary, using a complex and complete first-principles-based computational framework, we found there are dynamic lone pair electrons that are stereochemically active as the weak chemical bonding origin of rattling atoms and suppressed low-energy Einstein modes, which eventually drives large phonon anharmonicity and largely inhibits heat propagation. Meanwhile, the strong chemical bond hierarchy, with some atoms weakly bonding to the rest of the lattice, thermally induces the coexistence of soft crystalline sublattices, metavalent bonding, and fluctuating noncrystalline rattlers, leading to a mixed crystalline-liquid state and rattlinglike thermal damping. Finally, crystalline $Cs_3Bi_2I_6Cl_3$, with dual particle-wave behavior of the heat-carrying excitations, exhibits ultralow κ_L of $\sim$0.223 W m^{-1} K^{-1} at 300 K and glassy temperature-dependent thermal transport. We stress that this finding is a significant result in its own right by theory, as it represents the discovery of the heat transport mechanism for extremely low κ_L in halide perovskites.

IV. COMPUTATIONAL METHODS

First-principles calculations were performed within the framework of the Perdew-Burke-Ernzerhof generalized gradient approximation [65,66], as implemented in the Vienna *Ab initio* Simulation Package (VASP) [67,68]. The cutoff energy for the plane wave expansion was 500 eV on the 5 × 5 × 3 Γ-centered **k** mesh [69]. All structures were fully relaxed until the residual forces on each atom were less than 0.01 eV Å^{-1}. A 3 × 3 × 2 supercell with 252 atoms was used to calculate the harmonic phonon dispersion within the finite-displacement method using the PHONOPY code [70,71] bundled with VASP.

The molecular dynamics calculations were performed with a 3 × 3 × 2 supercell via a canonical ensemble using a Nosé-Hoover thermostat, which provided force and displacement for extracting renormalized force constants at high temperatures in the TDEP package [72–74]. A total of 50 ps with 1 fs/step for 300 K was calculated with a plane wave cutoff of 500 eV. The cutoff radii of the second-, third-, and fourth-order force constants were set as 15, 8.6, and 6.0 Å, respectively. The computation of the particlelike and wavelike contributions used the Wigner transport equation [28,29] as implemented in the PHONO3PY package [75–77], in which the force constants were converted from the TDEP format using our in-house scripts [78,79]. The thermal conductivity ($\kappa_L = \kappa_p + \kappa_c$) was computed based on a converged **q** mesh of 10 × 10 × 10.

ACKNOWLEDGMENTS

The authors acknowledge financial support from the Guangdong Basic and Applied Basic Research Foundation (Grant No. 2022A1515140030) and the National Natural Science Foundation of China (Grant No. 12104458). This work was also financially supported by the Postgraduate Education Reform and Quality Improvement Project of Henan Province (Grant No. YJS2023ZX19) and the National Natural Science Foundation of Henan Province of China (Grant No. 222300420416). The numerical calculations were performed at the Supercomputer Center of the China Spallation Neutron Source.

The authors declare there are no conflicts of interest.

APPENDIX A: ELECTRONIC LOCALIZATION FUNCTION ANALYSIS

The electron localization function (ELF), put forth by Becke and Edgecombe [80], can effectively describe the nature of chemical bonding in molecules and crystals empirically. In general, an ELF value close to 1 indicates fully localized electrons, and the zero region corresponds to a low electron density area. As shown for $Cs_3Bi_2I_6Cl_3$ in Fig. 6, the ELF values are zero between I and Cs/Cl atoms. They are about 0.4 between I and Bi atoms. This means I atoms form a delocalized bond with Bi atoms with a delocalized electron distribution.

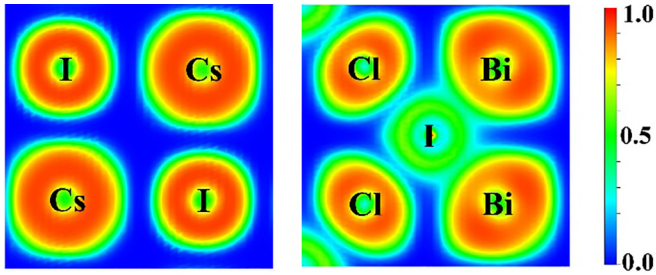

FIG. 6. Calculated electronic localization function maps parallel to the Cs-I-Cs (left) and Bi-I-Cl (right) planes. Red and blue regions refer to the highest (1.0) and lowest (0.0) values, indicating the fully localized electron area and the ultralow electron density area, respectively.

APPENDIX B: CONVERGENCE TEST OF κ_L

Here, we focus on the convergence of κ_L with respect to the Brillouin zone sampling density. Figure 7 shows the values of κ_L obtained along the in-plane and cross-plane directions. It seems that κ_L already reaches its converged value with the $10 \times 10 \times 10$ **q** grid used in this work.

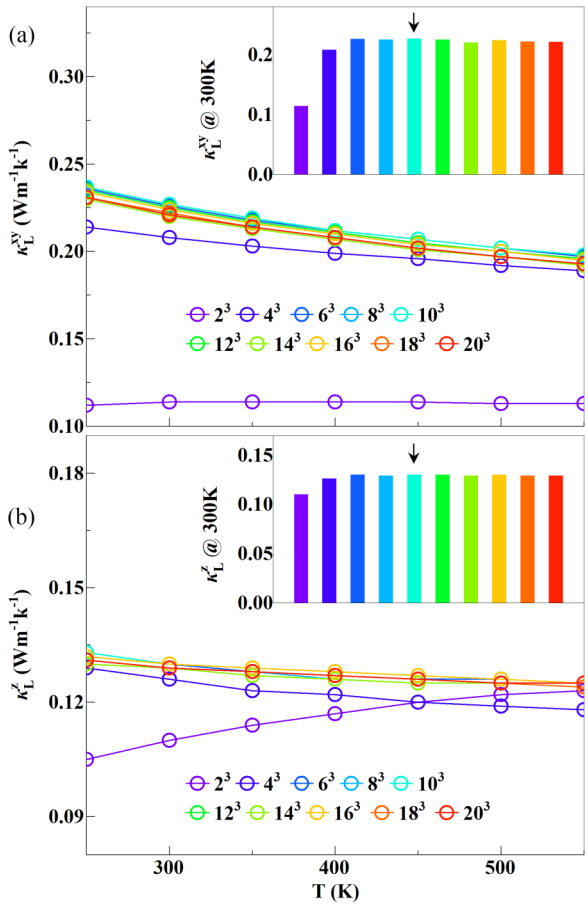

FIG. 7. Calculated temperature-dependent lattice thermal conductivity of $Cs_3Bi_2I_6Cl_3$ with $N \times N \times N$ (N^3, $N = 2$–20) **q** meshes along the (a) in-plane and (b) cross-plane directions. Inset: κ_L at $T = 300$ K for different **q** meshes. The black arrow in the inset of each plot indicates the **q** mesh used in the text.

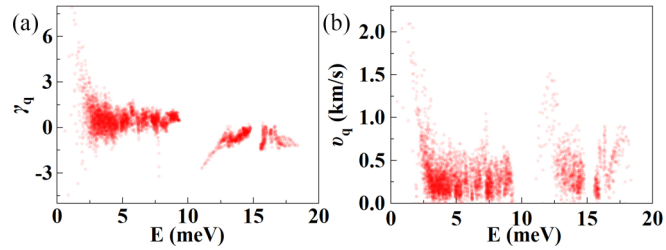

FIG. 8. Mode (a) Grüneinen parameters and (b) group velocity as a function of frequency for $Cs_3Bi_2I_6Cl_3$ at 300 K.

APPENDIX C: MODE GrüNEINEN PARAMETERS AND GROUP VELOCITY

The Grüneinen parameter γ can describe the anharmonic interactions of a crystal, which is useful for analyzing the physical nature of κ_L. In general, a large γ means strong phonon anharmonicity, which can greatly suppress heat transport and, accordingly, lead to low κ_L. Herein, we calculate the mode Grüneinen parameters of $Cs_3Bi_2I_6Cl_3$ and present them in Fig. 8. Figure 8 shows an unexpected large γ at around 2.5 meV in the low-energy zone dominated by the collective motions of Cs and I atoms. Acoustic modes and low-frequency optical modes strongly overlap in this zone. This will lead to ultralow κ_L since low-energy modes are mainly responsible for heat transport in semiconductors. According to the Boltzmann transport equation, κ_L is proportional to the group velocity. Here, we calculate mode group velocities using $\upsilon_{i,\mathbf{q}} = \frac{\partial \omega_{i,\mathbf{q}}}{\partial \mathbf{q}}$, where $\omega_{i,\mathbf{q}}$ is the phonon frequency. In Fig. 8(b), large $\upsilon_{i,\mathbf{q}}$ mainly locate near 2.5 meV in the low-energy zone, which is the same as γ in Fig. 8(a). All $\upsilon_{i,\mathbf{q}}$ are less than 2.5 km/s. Such low values of $\upsilon_{i,\mathbf{q}}$ can greatly lower κ_L of $Cs_3Bi_2I_6Cl_3$ [5].

APPENDIX D: MODE AND CUMULATIVE κ_p

The cumulative κ_p and their mode distribution are plotted in Fig. 9 with respect to frequency. Clearly, large values of mode κ_p can be found near 2.5 meV, similar to those of $\gamma_{i,\mathbf{q}}$ and $\upsilon_{i,\mathbf{q}}$. This range is made of acoustic and low-energy optical phonon modes, which dominate κ_p from particlelike phonon propagation in the Peierls-Boltzmann transport equation. The cumulative κ_p quickly reaches 72.8% and 79.1% with frequency below 5 meV along the in-plane and cross-plane directions, respectively.

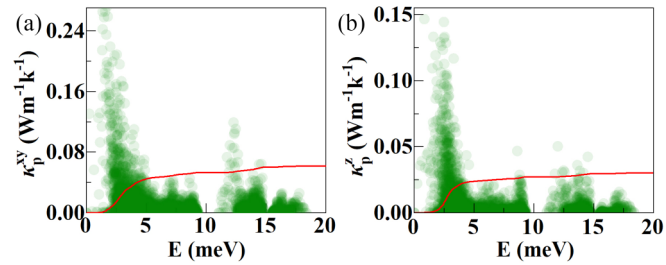

FIG. 9. Mode and cumulative κ_p of $Cs_3Bi_2I_6Cl_3$ at 300 K along the (a) in-plane and (b) cross-plane directions.

TABLE II. Calculated κ_L, κ_p, and κ_c (in $\mathrm{W\,m^{-1}\,K^{-1}}$) at 300 K for $Cs_3Bi_2I_6Cl_3$ with four-phonon interactions [83,84].

$\kappa_L^{xy}/\kappa_p^{xy}/\kappa_c^{xy}$	$\kappa_L^{z}/\kappa_p^{z}/\kappa_c^{z}$	Interaction
0.227/0.061/0.165	0.131/0.030/0.101	Three phonon
0.173/0.056/0.117	0.147/0.027/0.120	(3+4) phonon

APPENDIX E: EFFECT OF FOUR-PHONON INTERACTIONS ON κ_L

Recently, many studies supported the significant role of four-phonon scattering processes in heat transport [81,82]. Here, to check the effect in our system, we recalculate κ_L using the modified FOURPHONON [83], which contains four-phonon interactions and the off-diagonal terms of the heat-flux operator, an additional contribution of the lattice thermal conductivity κ_c. Table II shows the values of κ_L at 300 K with and without four-phonon interactions. For the in-plane direction, four-phonon scattering reduces the intrinsic κ_L^{xy} of $Cs_3Bi_2I_6Cl_3$. Conversely, κ_L^{z} slightly increases along the cross-plane direction, which seems counterintuitive. To see it, we revisit the formula for the Wigner transport equation [28,29]. For the particlelike phonon conduction, the equation, including both three-phonon and four-phonon scattering, can be described as

$$\kappa_{p,3+4} = \frac{1}{V}\sum_{\lambda} \upsilon^2 c_\lambda \left(\tau_{3,\lambda}^{-1} + \tau_{4,\lambda}^{-1}\right)^{-1}. \tag{E1}$$

Here, λ stands for the phonon mode $(\mathbf{q}, j)$ with j labeling the phonon dispersion branch. V is the crystal volume, υ is the phonon group velocity, and c_λ is phonon specific heat per mode. In this form, four-phonon scattering always reduces the intrinsic κ_p of solids by decreasing the phonon lifetime ($\tau^{-1} = \tau_3^{-1} + \tau_4^{-1}$) due to Fermi's golden rule [85]. It works well for the population conductivity in $Cs_3Bi_2I_6Cl_3$ (see Table II) and for materials in which particlelike phonon propagation dominates κ_L [85]. For wavelike phonon conduction, it depicts the off-diagonal terms of the heat-flux operator as

$$\kappa_c = \frac{\hbar^2}{k_B T^2 V N_0}\sum_{\mathbf{q}}\sum_{s\neq s'} \frac{\omega_{\mathbf{q}}^{s}+\omega_{\mathbf{q}}^{s'}}{2}\upsilon_{\mathbf{q}}^{s,s'}\upsilon_{\mathbf{q}}^{s',s} \times \frac{\omega_{\mathbf{q}}^{s} n_{\mathbf{q}}^{s}\left(n_{\mathbf{q}}^{s}+1\right)+\omega_{\mathbf{q}}^{s'} n_{\mathbf{q}}^{s'}\left(n_{\mathbf{q}}^{s'}+1\right)}{\frac{4(\omega_{\mathbf{q}}^{s}-\omega_{\mathbf{q}}^{s'})^2}{\Gamma_{\mathbf{q}}^{s}+\Gamma_{\mathbf{q}}^{s}}+\left(\Gamma_{\mathbf{q}}^{s}+\Gamma_{\mathbf{q}}^{s}\right)}. \tag{E2}$$

Clearly, the mode thermal conductivity from wavelike coherent phonons is

$$\kappa_{\mathbf{q},c} \propto \sum_{s\neq s'} \frac{A(\omega_{\mathbf{q}}, \upsilon_{\mathbf{q}}, n_{\mathbf{q}})}{\frac{4(\omega_{\mathbf{q}}^{s}-\omega_{\mathbf{q}}^{s'})^2}{\Gamma_{\mathbf{q}}^{s}+\Gamma_{\mathbf{q}}^{s}}+\left(\Gamma_{\mathbf{q}}^{s}+\Gamma_{\mathbf{q}}^{s}\right)}. \tag{E3}$$

Here, $\Gamma_{\mathbf{q}} = \tau_{\mathbf{q}}^{-1}$, and $A(\omega_{\mathbf{q}}, \upsilon_{\mathbf{q}}, n_{\mathbf{q}})$ is the prefactor independent of the phonon lifetime. In this case, adding four-phonon scattering decreases $\frac{4(\omega_{\mathbf{q}}^{s}-\omega_{\mathbf{q}}^{s'})^2}{\Gamma_{\mathbf{q}}^{s}+\Gamma_{\mathbf{q}}^{s}}$ and. conversely, increases $(\Gamma_{\mathbf{q}}^{s}+\Gamma_{\mathbf{q}}^{s})$. This means four-phonon scattering does not necessarily reduce the coherent thermal conductivity κ_c and has the potential to enhance the lattice thermal conductivity where wavelike tunneling of phonons is crucial in heat transport. In $Cs_3Bi_2I_6Cl_3$, we see that four-phonon scattering leads to an abnormal enhancement of the cross-plane thermal conductivity due to the increase in κ_c^{z}.

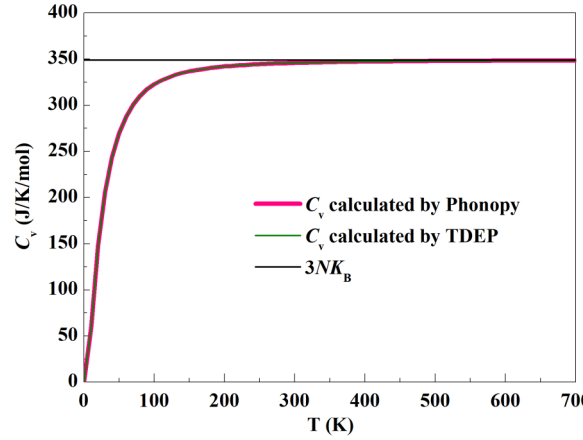

FIG. 10. Calculated heat capacity under constant volume of $Cs_3Bi_2I_6Cl_3$ as a function of temperature. The red and olive curves depict the values calculated by PHONOPY and TDEP, respectively. The black line indicates the classical limit ($3Nk_B$) of the phonon heat capacity.

APPENDIX F: HEAT CAPACITY AND THERMAL EXPANSION

In our work, the second-order force constant, used to produce the heat capacity, is directly computed from molecular dynamics simulations. This means our calculated heat capacity C_v is temperature dependent and contains phonon anharmonicity. To make this clear, we calculated the heat capacity using TDEP [72–74] and PHONOPY [70,71]. In Fig. 10, the two codes give the same result, and C_v eventually approaches $3Nk_B$ at high temperatures. In addition, to study the effect of thermal expansion on κ_L, NPT dynamics at 300 K are performed at atmosphere pressure. The lattice parameters are further calculated as the average in each simulation. Our computed $a = 8.62$ Å and $c = 10.52$ Å are larger than the initial values of $a = 8.43$ Å and $c = 10.29$ Å due to the thermal expansion effect. We then use the temperature-dependent lattice structure as the initial configuration using the same computational methods in the main text to calculate κ_L. The values of κ_L are 0.159 and 0.070 $\mathrm{W\,m^{-1}\,K^{-1}}$ along the in-plane and cross-plane directions, respectively, which is on the same order of magnitude as our initial result and the experiment.

APPENDIX G: TEMPERATURE-DEPENDENT PHONON DISPERSIONS

To check the effect of temperature-dependent force constants on κ_L, we perform molecular dynamics calculations at 500 K and recalculate κ_L using the same method described above. The temperature-dependent phonon dispersions are shown in Fig. 11. Figure 11 indicates that there is a downshift in high-energy mode frequency (above 10 meV) with the increase in temperature. As for low-energy phonons with

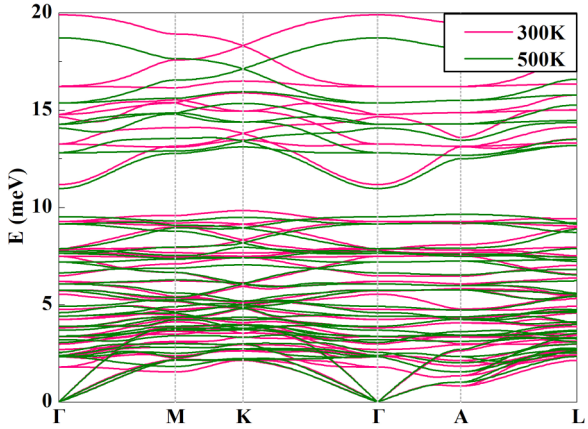

FIG. 11. Calculated temperature-dependent phonon dispersions at 300 K (pink) and 500 K (olive) for $Cs_3Bi_2I_6Cl_3$. The finite-temperature dispersions are calculated using the TDEP software from molecular dynamics at 300 and 500 K.

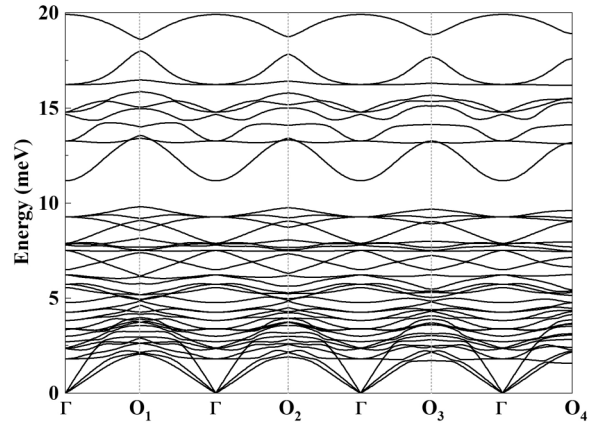

FIG. 12. Calculated phonon dispersion of $Cs_3Bi_2I_6Cl_3$ at 300 K along the off-symmetry directions. The off-symmetry points of O_1, O_2, O_3, and O_4 are (0.37, 0.25, 0), (0.4, 0.19, 0), (0.44, 0.12, 0), and (0.48, 0.04, 0), respectively. These points locate along the M-K line.

frequency below 10 meV, it is complicated and changeable at finite temperatures. The acoustic and low-energy optical modes unexpectedly harden at the Γ, M, A, and L points. Using temperature-dependent second and third force constants. Our calculated κ_L^{xy} (κ_L^z) at 500 K is 0.202 (0.126) and 0.198 (0.132) W m^{-1} K^{-1} using temperature-dependent second and third force constants from molecular dynamics at 300 and 500 K, respectively. These results indicate that it is reasonable to use the renormalized force constants from the simulations at 300 K to estimate κ_L at 500 K.

APPENDIX H: OFF-SYMMETRY PHONON DISPERSIONS

To check whether there is an imaginary phonon dispersion of $Cs_3Bi_2I_6Cl_3$ in the whole Brillouin zone, we calculate the phonon dispersion along selected off-symmetry directions, Γ-O_i (i = 1–4), where O_i is the point along the M-K line. As shown in Fig. 12, there are no negative frequencies, agreeing with the result for phonon dispersions along high-symmetry lines.

[1] L. Li, W.-D. Liu, Q. Liu, and Z.-G. Chen, Multifunctional wearable thermoelectrics for personal thermal management, Adv. Funct. Mater. **32**, 2200548 (2022).

[2] F. Li, L. Zhou, J.-X. Liu, Y. Liang, and G.-J. Zhang, High-entropy pyrochlores with low thermal conductivity for thermal barrier coating materials, J. Adv. Ceram. **8**, 576 (2019).

[3] W.-Y. Chen, X.-L. Shi, J. Zou, and Z.-G. Chen, Thermoelectric coolers: Progress, challenges, and opportunities, Small Methods **6**, 2101235 (2022).

[4] T. Ghosh, M. Dutta, D. Sarkar, and K. Biswas, Insights into low thermal conductivity in inorganic materials for thermoelectrics, J. Am. Chem. Soc. **144**, 10099 (2022).

[5] B. Qin, D. Wang, and L.-D. Zhao, Slowing down the heat in thermoelectrics, InfoMat **3**, 755 (2021).

[6] G. S. Nolas, D. T. Morelli, and T. M. Tritt, SKUTTERUDITES: A phonon-glass-electron crystal approach to advanced thermoelectric energy conversion applications, Annu. Rev. Mater. Sci. **29**, 89 (1999).

[7] T. Takabatake, K. Suekuni, T. Nakayama, and E. Kaneshita, Phonon-glass electron-crystal thermoelectric clathrates: Experiments and theory, Rev. Mod. Phys. **86**, 669 (2014).

[8] R. Chetty, A. Bali, and R. C. Mallik, Tetrahedrites as thermoelectric materials: An overview, J. Mater. Chem. C **3**, 12364 (2015).

[9] K. Zhao, P. Qiu, X. Shi, and L. Chen, Recent advances in liquid-like thermoelectric materials, Adv. Funct. Mater. **30**, 1903867 (2020).

[10] K. Zhao, A. B. Blichfeld, H. Chen, Q. Song, T. Zhang, C. Zhu, D. Ren, R. Hanus, P. Qiu, B. B. Iversen, F. Xu, G. J. Snyder, X. Shi, and L. Chen, Enhanced thermoelectric performance through tuning bonding energy in $Cu_2Se_{1Cx}S_x$ liquid-like materials, Chem. Mater. **29**, 6367 (2017).

[11] H. Liu, X. Shi, F. Xu, L. Zhang, W. Zhang, L. Chen, Q. Li, C. Uher, T. Day, and G. J. Snyder, Copper ion liquid-like thermoelectrics, Nat. Mater. **11**, 422 (2012).

[12] B. Li, H. Wang, Y. Kawakita, Q. Zhang, M. Feygenson, H. L. Yu, D. Wu, K. Ohara, T. Kikuchi, K. Shibata, T. Yamada, X. K. Ning, Y. Chen, J. Q. He, D. Vaknin, R. Q. Wu, K. Nakajima, and M. G. Kanatzidis, Liquid-like thermal conduction in intercalated layered crystalline solids, Nat. Mater. **17**, 226 (2018).

[13] C. Wang, R. Cheng, and Y. Chen, Theoretical evaluation of the persistence of transverse phonons across a liquid-like transition in superionic conductor KAg_3Se_2, Chem. Mater. **35**, 1780 (2023).

[14] S. Lin, W. Li, and Y. Pei, Thermally insulative thermoelectric argyrodites, Mater. Today **48**, 198 (2021).

[15] Md A. Haque, S. Kee, D. R. Villalva, W.-L. Ong, and D. Baran, Halide perovskites: Thermal transport and prospects for thermoelectricity, Adv. Sci. **7**, 1903389 (2020).

[16] A. Younis, C.-H. Lin, X. Guan, S. Shahrokhi, C.-Y. Huang, Y. Wang, T. He, S. Singh, L. Hu, J. R. D. Retamal, J.-H. He, and T. Wu, Halide perovskites: A new era of solution-processed electronics, Adv. Mater. **33**, 2005000 (2021).

[17] C. Liu, W. Huhn, K.-Z. Du, A. Vazquez-Mayagoitia, D. Dirkes, W. You, Y. Kanai, D. B. Mitzi, and V. Blum, Tunable semiconductors: Control over carrier states and excitations in layered hybrid organic-inorganic perovskites, Phys. Rev. Lett. **121**, 146401 (2018).

[18] W. Lee, H. Li, A. B. Wong, D. Zhang, M. Lai, Y. Yu, Q. Kong, E. Lin, J. J. Urban, J. C. Grossman, and P. Yang, Ultralow thermal conductivity in all-inorganic halide perovskites, Proc. Natl. Acad. Sci. USA **114**, 8693 (2017).

[19] A. H. Slavney, L. Leppert, A. Saldivar Valdes, D. Bartesaghi, T. J. Savenije, J. B. Neaton, and H. I. Karunadasa, Small-band-gap halide double perovskites, Angew. Chem., Int. Ed. **57**, 12765 (2018).

[20] Y. Ling, Z. Yuan, Y. Tian, X. Wang, J. C. Wang, Y. Xin, K. Hanson, B. Ma, and H. Gao, Bright light-emitting diodes based on organometal halide perovskite nanoplatelets, Adv. Mater. **28**, 305 (2016).

[21] S. Shrestha, R. Fischer, G. J. Matt, P. Feldner, T. Michel, A. Osvet, I. Levchuk, B. Merle, S. Golkar, H. Chen, S. F. Tedde, O. Schmidt, R. Hock, M. Rührig, M. Göken, W. Heiss, G. Anton, and C. J. Brabec, High-performance direct conversion x-ray detectors based on sintered hybrid lead triiodide perovskite wafers, Nat. Photonics **11**, 436 (2017).

[22] S. P. Senanayak, B. Yang, T. H. Thomas, N. Giesbrecht, W. Huang, E. Gann, B. Nair, K. Goedel, S. Guha, X. Moya, C. R. McNeill, P. Docampo, A. Sadhanala, R. H. Friend, and H. Sirringhaus, Understanding charge transport in lead iodide perovskite thin-film field-effect transistors, Sci. Adv. **3**, e1601935 (2017).

[23] J. Y. Kim, J.-W. Lee, H. S. Jung, H. Shin, and N.-G. Park, High-efficiency perovskite solar cells, Chem. Rev. **120**, 7867 (2020).

[24] Y. Zhang, C. Y. Tso, J. S. Iñigo, S. Liu, H. Miyazaki, C. Y. H. Chao, and K. M. Yu, Perovskite thermochromic smart window: Advanced optical properties and low transition temperature, Appl. Energy **254**, 113690 (2019).

[25] Q. Zhang, R. Su, W. Du, X. Liu, L. Zhao, S. T. Ha, and Q. Xiong, Advances in small perovskite-based lasers, Small Methods **1**, 1700163 (2017).

[26] K. M. McCall, C. C. Stoumpos, O. Y. Kontsevoi, G. C. B. Alexander, B. W. Wessels, and M. G. Kanatzidis, From 0D $Cs_3Bi_2I_9$ to 2D $Cs_3Bi_2I_6Cl_3$: Dimensional expansion induces a direct band gap but enhances electron–phonon coupling, Chem. Mater. **31**, 2644 (2019).

[27] P. Acharyya, T. Ghosh, K. Pal, K. S. Rana, M. Dutta, D. Swain, M. Etter, A. Soni, U. V. Waghmare, and K. Biswas, Glassy thermal conductivity in $Cs_3Bi_2I_6Cl_3$ single crystal, Nat. Commun. **13**, 5053 (2022).

[28] M. Simoncelli, N. Marzari, and F. Mauri, Wigner formulation of thermal transport in solids, Phys. Rev. X **12**, 041011 (2022).

[29] M. Simoncelli, N. Marzari, and F. Mauri, Unified theory of thermal transport in crystals and glasses, Nat. Phys. **15**, 809 (2019).

[30] E. Yu. Peresh, V. I. Sidei, O. V. Zubaka, and I. P. Stercho, $K_2(Rb_2, Cs_2, Tl_2)TeBr_6(I_6)$ and $Rb_3(Cs_3)Sb_2(Bi_2)Br_9(I_9)$ perovskite compounds, Inorg. Mater. **47**, 208 (2011).

[31] K. K. Bass, L. Estergreen, C. N. Savory, J. Buckeridge, D. O. Scanlon, P. I. Djurovich, S. E. Bradforth, M. E. Thompson, and B. C. Melot, Vibronic structure in room temperature photoluminescence of the halide perovskite $Cs_3Bi_2Br_9$, Inorg. Chem. **56**, 42 (2017).

[32] K. Momma and F. Izumi, VESTA 3 for three-dimensional visualization of crystal, volumetric and morphology data, J. Appl. Cryst. **44**, 1272 (2011).

[33] J. Klarbring, O. Hellman, I. A. Abrikosov, and S. I. Simak, Anharmonicity and ultralow thermal conductivity in lead-free halide double perovskites, Phys. Rev. Lett. **125**, 045701 (2020).

[34] R. X. Yang, J. M. Skelton, E. L. da Silva, J. M. Frost, and A. Walsh, Assessment of dynamic structural instabilities across 24 cubic inorganic halide perovskites, J. Chem. Phys. **152**, 024703 (2020).

[35] A. Togo and I. Tanaka, First principles phonon calculations in materials science, Scr. Mater. **108**, 1 (2015).

[36] L. Monacelli and N. Marzari, First-principles thermodynamics of $CsSnI_3$, Chem. Mater. **35**, 1702 (2023).

[37] H. Liu, J. Yang, X. Shi, S. A. Danilkin, D. Yu, C. Wang, W. Zhang, and L. Chen, Reduction of thermal conductivity by low energy multi-einstein optic modes, J. Materiomics **2**, 187 (2016).

[38] V. Keppens, D. Mandrus, B. C. Sales, B. C. Chakoumakos, P. Dai, R. Coldea, M. B. Maple, D. A. Gajewski, E. J. Freeman, and S. Bennington, Localized vibrational modes in metallic solids, Nature (London) **395**, 876 (1998).

[39] C. Chakravarty, P. G. Debenedetti, and F. H. Stillinger, Lindemann measures for the solid-liquid phase transition, J. Chem. Phys. **126**, 204508 (2007).

[40] K. Miyata, T. L. Atallah, and X.-Y. Zhu, Lead halide perovskites: Crystal-liquid duality, phonon glass electron crystals, and large polaron formation, Sci. Adv. **3**, e1701469 (2017).

[41] W. Qiu, L. Xi, P. Wei, X. Ke, J. Yang, and W. Zhang, Part-crystalline part-liquid state and rattling-like thermal damping in materials with chemical-bond hierarchy, Proc. Natl. Acad. Sci. USA **111**, 15031 (2014).

[42] P. Ying, X. Li, Y. Wang, J. Yang, C. Fu, W. Zhang, X. Zhao, and T. Zhu, Hierarchical chemical bonds contributing to the intrinsically low thermal conductivity in α-MgAgSb thermoelectric materials, Adv. Funct. Mater. **27**, 1604145 (2017).

[43] K. N. Lad and A. Pratap, Velocity autocorrelation function for simple liquids and its application to liquid metals and alloys, Phys. Rev. E **70**, 051201 (2004).

[44] M. M. Koza, M. R. Johnson, R. Viennois, H. Mutka, L. Girard, and D. Ravot, Breakdown of phonon glass paradigm in La- and Ce-filled Fe_4Sb_{12} skutterudites, Nat. Mater. **7**, 805 (2008).

[45] L. Xie, D. Wu, H. Yang, Y. Yu, Y. Wang, and J. He, Direct atomic-scale observation of the Ag^+ diffusion structure in the quasi-2D "liquid-like" state of superionic thermoelectric $AgCrSe_2$, J. Mater. Chem. C **7**, 9263 (2019).

[46] C. Tang, Z. Huang, J. Pei, B.-P. Zhang, P.-P. Shang, Z. Shan, Z. Zhang, H. Gu, and K. Wen, Bi_2Te_3 single crystals with high room-temperature thermoelectric performance enhanced by manipulating point defects based on first-principles calculation, RSC Adv. **9**, 14422 (2019).

[47] D. G. Cahill and R. O. Pohl, Lattice vibrations and heat transport in crystals and glasses, Annu. Rev. Phys. Chem. **39**, 93 (1988).

[48] Y. Xia, V. Ozoliņš, and C. Wolverton, Microscopic mechanisms of glasslike lattice thermal transport in cubic $Cu_{12}Sb_4S_{13}$ tetrahedrites, Phys. Rev. Lett. **125**, 085901 (2020).

[49] M. Beekman, D. T. Morelli, and G. S. Nolas, Better thermoelectrics through glass-like crystals, Nat. Mater. **14**, 1182 (2015).

[50] P. B. Allen and J. L. Feldman, Thermal conductivity of disordered harmonic solids, Phys. Rev. B **48**, 12581 (1993).

[51] G. Caldarelli, M. Simoncelli, N. Marzari, F. Mauri, and L. Benfatto, Many-body Green's function approach to lattice thermal transport, Phys. Rev. B **106**, 024312 (2022).

[52] D. Dangić, O. Hellman, S. Fahy, and I. Savić, The origin of the lattice thermal conductivity enhancement at the ferroelectric phase transition in GeTe, npj Comput. Mater. **7**, 57 (2021).

[53] E. S. Toberer, A. Zevalkink, and G. J. Snyder, Phonon engineering through crystal chemistry, J. Mater. Chem. **21**, 15843 (2011).

[54] Z. Zeng, C. Chen, C. Zhang, Q. Zhang, and Y. Chen, Critical phonon frequency renormalization and dual phonon coexistence in layered Ruddlesden-Popper inorganic perovskites, Phys. Rev. B **105**, 184303 (2022).

[55] B. Silvi and A. Savin, Classification of chemical bonds based on topological analysis of electron localization functions, Nature (London) **371**, 683 (1994).

[56] T. H. Dunning, D. E. Woon, J. Leiding, and L. Chen, The first row anomaly and recoupled pair bonding in the halides of the late p-block elements, Acc. Chem. Res. **46**, 359 (2013).

[57] E. R. Johnson, S. Keinan, P. Mori-Sánchez, J. Contreras-García, A. J. Cohen, and W. Yang, Revealing noncovalent interactions, J. Am. Chem. Soc. **132**, 6498 (2010).

[58] J.-Y. Raty, M. Schumacher, P. Golub, V. L. Deringer, C. Gatti, and M. Wuttig, A quantum-mechanical map for bonding and properties in solids, Adv. Mater. **31**, 1806280 (2019).

[59] M. D. Nielsen, V. Ozolins, and J. P. Heremans, Lone pair electrons minimize lattice thermal conductivity, Energy Environ. Sci. **6**, 570 (2013).

[60] T. A. Manz and N. G. Limas, Introducing DDEC6 atomic population analysis: Part 1. Charge partitioning theory and methodology, RSC Adv. **6**, 47771 (2016).

[61] N. G. Limas and T. A. Manz, Introducing DDEC6 atomic population analysis: Part 2. Computed results for a wide range of periodic and nonperiodic materials, RSC Adv. **6**, 45727 (2016).

[62] T. A. Manz, Introducing DDEC6 atomic population analysis: Part 3. Comprehensive method to compute bond orders, RSC Adv. **7**, 45552 (2017).

[63] B. J. Kooi and M. Wuttig, Chalcogenides by design: Functionality through metavalent bonding and confinement, Adv. Mater. **32**, 1908302 (2020).

[64] L. Elalfy, D. Music, and M. Hu, Metavalent bonding induced abnormal phonon transport in diamondlike structures: Beyond conventional theory, Phys. Rev. B **103**, 075203 (2021).

[65] J. P. Perdew, K. Burke, and M. Ernzerhof, Generalized gradient approximation made simple, Phys. Rev. Lett. **77**, 3865 (1996).

[66] G. Kresse and D. Joubert, From ultrasoft pseudopotentials to the projector augmented-wave method, Phys. Rev. B **59**, 1758 (1999).

[67] G. Kresse and J. Furthmüller, Efficient iterative schemes for *ab initio* total-energy calculations using a plane-wave basis set, Phys. Rev. B **54**, 11169 (1996).

[68] G. Sun, J. Kürti, P. Rajczy, M. Kertesz, J. Hafner, and G. Kresse, Performance of the Vienna *Ab initio* Simulation Package (VASP) in chemical applications, J. Mol. Struct.: THEOCHEM **624**, 37 (2003).

[69] H. J. Monkhorst and J. D. Pack, Special points for Brillouin-zone integrations, Phys. Rev. B **13**, 5188 (1976).

[70] L. Chaput, A. Togo, I. Tanaka, and G. Hug, Phonon-phonon interactions in transition metals, Phys. Rev. B **84**, 094302 (2011).

[71] K. Parlinski, Z. Q. Li, and Y. Kawazoe, First-principles determination of the soft mode in cubic ZrO_2, Phys. Rev. Lett. **78**, 4063 (1997).

[72] O. Hellman, I. A. Abrikosov, and S. I. Simak, Lattice dynamics of anharmonic solids from first principles, Phys. Rev. B **84**, 180301(R) (2011).

[73] O. Hellman and I. A. Abrikosov, Temperature-dependent effective third-order interatomic force constants from first principles, Phys. Rev. B **88**, 144301 (2013).

[74] O. Hellman, P. Steneteg, I. A. Abrikosov, and S. I. Simak, Temperature dependent effective potential method for accurate free energy calculations of solids, Phys. Rev. B **87**, 104111 (2013).

[75] A. Togo, L. Chaput, and I. Tanaka, Distributions of phonon lifetimes in Brillouin zones, Phys. Rev. B **91**, 094306 (2015).

[76] A. Togo, First-principles phonon calculations with phonopy and phono3py, J. Phys. Soc. Jpn. **92**, 012001 (2023).

[77] L. Chaput, Direct solution to the linearized phonon Boltzmann equation, Phys. Rev. Lett. **110**, 265506 (2013).

[78] Z. Tong, Y. Zhang, A. Pecchia, C. Yam, L. Zhou, T. Dumitrică, and T. Frauenheim, Predicting the lattice thermal conductivity in nitride perovskite $LaWN_3$ from *ab initio* lattice dynamics, Adv. Sci. **10**, 2205934 (2023).

[79] H. Shao, D. Ding, Y. Fang, W. Song, J. Huang, C. Dong, and H. Zhang, Phonon transport in Cu_2GeSe_3: Effects of spin-orbit coupling and higher-order phonon-phonon scattering, Phys. Rev. B **107**, 085202 (2023).

[80] A. D. Becke and K. E. Edgecombe, A simple measure of electron localization in atomic and molecular systems, J. Chem. Phys. **92**, 5397 (1990).

[81] F. Eriksson, E. Fransson, and P. Erhart, The hiphive package for the extraction of high-order force constants by machine learning, Adv. Theor. Simul. **2**, 1800184 (2019).

[82] Y. Xia, K. Pal, J. He, V. Ozoliņš, and C. Wolverton, Particlelike phonon propagation dominates ultralow lattice thermal conductivity in crystalline Tl_3VSe_4, Phys. Rev. Lett. **124**, 065901 (2020).

[83] Z. Han, X. Yang, W. Li, T. Feng, and X. Ruan, FourPhonon: An extension module to ShengBTE for computing four-phonon scattering rates and thermal conductivity, Comput. Phys. Commun. **270**, 108179 (2022).

[84] W. Li, J. Carrete, N. A. Katcho, and N. Mingo, ShengBTE: A solver of the Boltzmann transport equation for phonons, Comput. Phys. Commun. **185**, 1747 (2014).

[85] T. Feng, L. Lindsay, and X. Ruan, Four-phonon scattering significantly reduces intrinsic thermal conductivity of solids, Phys. Rev. B **96**, 161201(R) (2017).